



Defect detection in composites by deep learning using solitary waves

Sangyoung Yoon^a, Amang (Song-Kyoo) Kim^b, Wesley J. Cantwell^c, Chan Yeob Yeun^b, Chung-Suk Cho^a, Young-Ji Byon^a, Tae-Yeon Kim^{a,*}

^a Department of Civil Infrastructure and Environmental Engineering, Khalifa University of Science and Technology, 127788, Abu Dhabi, United Arab Emirates

^b C2PS, Department of Electrical Engineering and Computer Science, Khalifa University of Science and Technology, 127788, Abu Dhabi, United Arab Emirates

^c Advanced Research & Innovation Center (ARIC), Khalifa University of Science and Technology, 127788, Abu Dhabi, United Arab Emirates



ARTICLE INFO

Keywords:
 AS4/PEEK
 Composite
 Convolutional neural networks
 Defect detection
 Granular crystal
 Machine Learning
 Non-destructive evaluation
 Solitary wave
 Artificial intelligence

ABSTRACT

This paper proposes a real-time non-destructive evaluation technique to detect defects in laminated composites by deep learning using highly nonlinear solitary waves (HNSWs). HNSW data are collected by conducting experiments using a granular crystal sensor composed of a vertical array of steel beads directly contacting an AS4/PEEK composite plate. Using HNSW data, a deep learning algorithm based on the convolution neural networks (CNN) is trained and tested for the identification of delamination in AS4/PEEK composites. The influence of the number of hidden layers and various CNN parameters is investigated for improved classification accuracy of the deep learning algorithm. A general curve fit is presented in order to facilitate the correct choice of the input pixel and batch size. Moreover, a multiple mode testing scheme, classifying defects using multiple HNSW signals, is introduced to improve the accuracy of the algorithm. The efficiency and accuracy of using three different types of the input signal (i.e., original (without pre-processing) and time-sliced/time-sliced noise-cutting signals (with pre-processing)) are examined for the real-time detection of defects. Mathematical formulations are established to obtain time-sliced and time-sliced noise-cutting signals from the original HNSW signals. It was found that accuracy could be improved by increasing both the number of hidden layers and the input pixel size, reducing the learning rate, and by using a batch normalization process and RELU activation function. For all three input signals, accuracy levels of over 90% were achieved in identifying the existence and location of delamination in AS4/PEEK composites, highlighting the possibility of using the proposed deep learning algorithm for the real-time detection of defects in laminated composites.

1. Introduction

Fiber-reinforced polymer (FRP) composites offer superior strength combined with lightweight and exhibit a high corrosion resistance compared with conventional metallic materials [1,2]. Such distinct features allow their use in various advanced engineering structures, such as spacecraft and aircraft, biomedical and chemical devices, automobiles, and buildings and bridges in civil structures. Amongst the various FRP composites, of particular interest in this study is the APC-2/S4 polyether ether ketone (AS4/PEEK) composite, which is a high-performance thermoplastic composite material consisting of a PEEK matrix reinforced with AS4 carbon fibers. AS4/PEEK composites have attracted considerable interest in the aerospace and defense industries, due to their high interlaminar fracture toughness and impact resistance, relative to conventional epoxy-based composites [3,4]. However, the detection of small defects and the determination of the

bond strength in an efficient and fast manner is challenging in laminated composites. Moreover, conventional detection methods [5–12] require bulky equipment, high power radiation, and/or a significant amount of data processing. Such drawbacks prevent these existing methods from the in-situ and rapid detection of defects in composite structures. To overcome these difficulties, as an alternative non-destructive evaluation (NDE) technique, this study introduces the application of deep learning (DL) to explore highly nonlinear solitary waves (HNSWs) generated from a granular crystal sensor for the accurate and efficient detection of defects in laminated composites in a fast and reliable manner in real-time.

Recently, granular crystal sensors have been introduced as an attractive alternative NDE method to existing techniques (e.g., ultrasound and X-ray) due to their simplicity, low cost, portability and energy efficiency. The sensor is comprised of a vertically aligned one-dimensional chain of spherical steel beads directly contacting an

* Corresponding author.

E-mail address: taeyeon.kim@ku.ac.ae (T.-Y. Kim).

inspection medium [13–15]. The chain supports the formation and propagation of HNSWs generated by the impact of the striker bead. In contrast to harmonic oscillatory waves in linear elastic media, HNSWs have the unique characteristic features such as a compact waveform, a tailororable wave speed, and high energy intensity [15–18]. Recent studies [13,17,19,20] have shown that HNSWs reflected through the interaction with an inspection medium retains a compact waveform without significant dispersion or attenuation, and they are highly sensitive to the mechanical and geometrical properties of the inspected medium.

By taking advantage of such sensitivity and the advantages of HNSWs, the HNSW-based diagnostic scheme has been successfully applied to weak bond and delamination detection in carbon fiber reinforced polymer (CFRP) laminates [21–23], disbond detection in honeycomb composite sandwich structures [24], matrix cracking in composite plates [25], and void detection in elastic solids [26]. Moreover, it has been applied for the non-destructive testing of bond quality of adhesively-bonded aluminum lap-joints [27], hydration monitoring of fresh concrete [28], the measurement of site-specific bone properties [29–32], the evaluation of implant stability in total hip arthroplasty [33], the detection of localized corrosion in steel plates [34–36], and the basic mechanical properties in composite beams [37] and rigid polyurethane foams [38]. Motivated by these successful applications of the granular crystal sensor system, the objective of this study is to develop a DL-based real-time NDE technique for the detection of defects in laminated composites using HNSWs. The DL-based NDE method uses a HNSW dataset generated through the reflection of solitary waves from composites using a granular crystal sensor. The proposed method takes advantage of the characteristic features and high sensitivity of HNSWs and the advantages of the granular crystal sensor described in the previous paragraph. Using a granular crystal sensor without DL requires an explicit analysis of the specific features, such as wave speed and/or amplitude, of the reflected HNSWs for the detection of defects. However, the proposed DL-based NDE technique can efficiently and accurately detect defects without explicitly analysing the characteristic features of the reflected HNSWs. In other words, the presence and location of defects in composites can be detected automatically using only the information associated with the input data.

Over the past two decades, artificial intelligence techniques have been dramatically improved and various machine learning algorithms including DL (i.e., artificial neural networks, CNN, etc.) have been developed [39–43]. Among the range of DL algorithms, we employ the CNN approach, which was specifically designed for image recognition with a very high degree of accuracy. As a result, the CNN approach has been widely adopted as the primary choice of DL techniques and its variants have been successfully proven in classification tasks across different domains [44–46]. With regard to NDE, the CNN approach has been applied to automatically detect and classify defects in various engineering materials and structures, such as steel [47,48], rail surfaces [49,50], tires [51], welds [52], and heat exchanger tubes [53]. Applications of CNN in composite materials have focused on detecting and monitoring internal damage using data from various NDE techniques. Examples include signals from ultrasonic methods to detect voids and delamination in CFRP [54,55], cracking in glass fiber reinforced polymers (GFRP) [56], X-ray computed tomography images to identify delamination in CFRP [57], cracking in silicon carbide (SiC) matrix composites [58], voids and inclusions in spacecraft composite structures [59], acoustic emission signals for detecting delamination and cracks in CFRP [60,61] as well as cracking in GFRP [62]. Moreover, thermographic images from infrared thermography have been used to detect debonds in CFRP using a spatial and temporal DL architecture [63], surface defects in GFRP [64], and various shapes of defect in composite laminates by applying Faster RCNN (Region based CNN) [65]. In this study, we explore the possibility of using HNSWs as the input data of the CNN for the identification of delamination in laminated composites. Importantly, HNSWs have a simple image pattern (see Fig. 3), which is a

compact waveform without significant dispersion with the interaction of an inspection medium. Such a simple image pattern of the HNSW makes the CNN easy to find patterns in HNSW signal images and classify the properties of an inspection medium in a fast and reliable manner.

The main contributions of this study can be summarized as follows. For the real-time detection of defects in laminated composites, a CNN architecture is developed using HNSW signals obtained from a granular crystal sensor. Moreover, for a more efficient and accurate detection of defects, we perform pre-processing to obtain time-sliced and time-sliced noise-cutting signals from original HNSW signals. Then, we examine the influence of three different types of the HNSW input signal (i.e., original, time-sliced, and time-sliced noise-cutting signals) on the accuracy of detecting defects is investigated. In addition, the effect of varying various CNN parameters (i.e., hidden layer, learning rate, activation function, dropout, input pixel size, batch size, and filter size) on classification accuracy are investigated. We also provide a simple mathematical relation between accuracy and the input pixel size and batch size for the improvement of the accuracy of the developed CNN architecture. Furthermore, a multiple mode testing scheme that classifies a defect in a composite using multiple HNSW signals is developed to improve the accuracy of the CNN architecture.

The remainder of this paper is organized as follows. In Section 2, we provide the experimental setup of the granular crystal sensor used to collect the HNSW dataset along with details of the pre-processing of input data to improve its efficiency and accuracy. In Section 3, we describe an architecture of the proposed CNN algorithm. In Section 4, the proposed CNN algorithm is trained and tested for the identification of the presence of the defect and the location of the defect in the composite. Finally, a number of conclusions and a summary are provided in Section 5.

2. Experimental setup for the DL algorithm

This section describes the experimental setup of the granular crystal sensor used to collect the HNSW dataset. The section also discusses the use of three different types of HNSW input signal for training and testing the DL-NDE technique.

2.1. Experimental setup for HNSWs dataset

A brief description of the experimental setup of the granular crystal sensor is provided and more details are given elsewhere [66]. Experiments were performed on four types of AS4/PEEK composite specimen, three of which contained a 20 mm diameter artificial defect placed at different locations through the thickness and the fourth being a pristine sample without a defect (see Fig. 1). Each sample was manufactured from 8 sheets of prepreg (thickness of 0.125 mm), supplied in a continuous roll. The sheets were cut to dimensions of 50 × 100mm, wrapped in a 50 µm thick polyimide film and placed in a metal mold. To create an artificial delamination, a polyamide film, with a diameter of 20 mm is placed between plies at specific interfaces. The metal mold was placed in a Meyer press and heated to 380 °C at a heating rate of approximately 20 °C/min, then slowly cooled to room temperature. As shown in Fig. 1b, three samples with artificial delaminations are labelled as A, B, and C, depending on the location of the defect.

Fig. 2 shows the experimental setup along with a schematic diagram of the sensor. The sensor is made of a one-dimensional chain of 21 vertically-aligned spherical particles (or beads) that are made from hardened AISI 52,100 steel. They are supported by four stainless steel guiding rods, and the last particle of the chain is in direct contact with the AS4/PEEK composite sample. To generate a HNSW in the granular chain, the striker particle at the top of the chain is dropped onto the rest of the chain from a height of 25 mm. Upon impact of the striker bead, a single incident HNSW is generated and propagates through the chain, which is measured by the sensor particle located in the middle of the chain (11th particle position from the top including the striker bead).

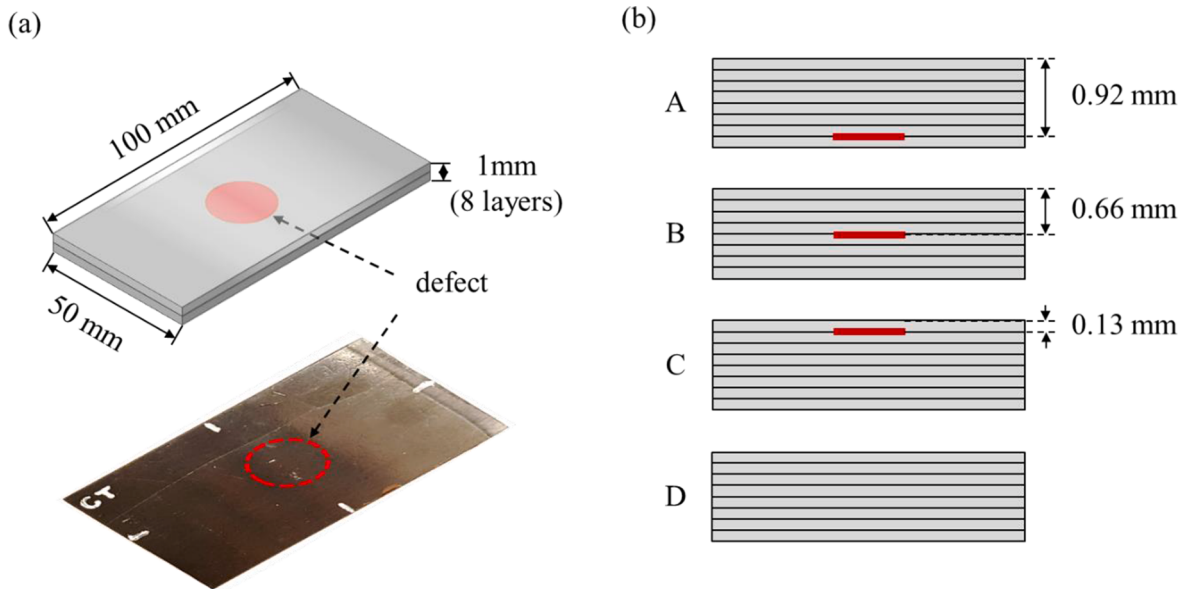


Fig. 1. (a) (Top) Graphical illustration of the 8 layer AS4/PEEK laminated composites with dimensions of 100 mm x 50 mm x 1 mm. The purple circle represents a defect created by placing a 20 mm diameter, 0.125 mm thick polyamide film between specific layers. (Bottom) A fabricated AS4/PEEK composite sample containing a defect (red circle). (b) Three samples labelled A, B, and C with defects located at three different interfaces and one pristine specimen labelled D without a defect. The defect depths in A, B, and C are 0.92 mm, 0.66 mm, and 0.13 mm from the top surface, respectively.

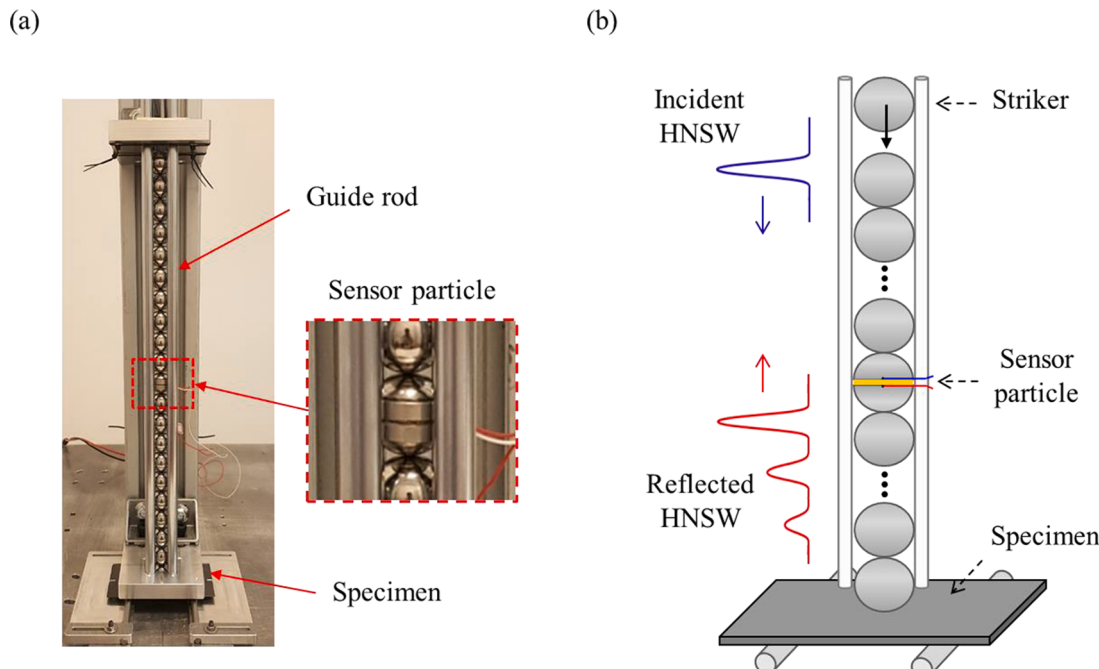


Fig. 2. (a) An experimental setup of a granular crystal sensor is made of a one-dimensional chain of 21 vertically aligned steel particles supported by steel guiding rods and a piezoelectric sensor embedded in the sensor particle to record HNSWs. The lowermost bead is in direct contact with the test specimen. (b) A schematic diagram of the granular crystal sensor showing the incident HNSW generated by the impact of a striker particle at the top and the HNSWs reflected from an inspection specimen.

The piezoelectric ceramic disk embedded in the sensor bead generates a voltage proportional to the compressive force applied to the disk. The temporal profiles of HNSWs generated from the sensor are recorded by an oscilloscope.

2.2. Dataset collection

Using the experimental setup of the granular crystal sensor described

in the previous section, the temporal profiles of the HNSW recorded in the embedded sensor bead are collected from each of four different types of AS4/PEEK laminate illustrated in Fig. 1b. Notice that the granular crystal sensor is located directly above the defect area. All HNSW data for training and classification for each sample are obtained through repeated experiments. Each HNSW datum has 40,001 V inputs versus time measured by the sensor particle during interaction with the AS4/PEEK composite as shown in Fig. 3a. In Fig. 3b, the first impulse

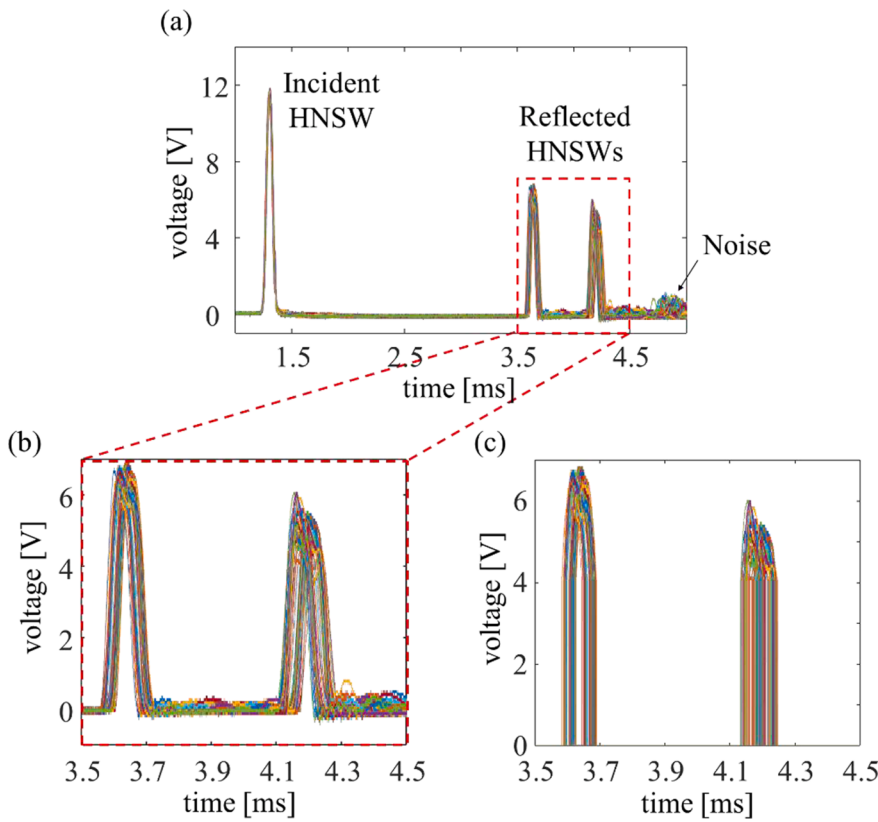


Fig. 3. (a) Original (raw) HNSW signals, measured by a granular crystal sensor, consisting of incident HNSWs generated by the impact of a striker particle and the reflected HNSWs generated by the interaction between AS4/PEEK composite specimens and the last particle of the granular crystal sensor. (b) Time-sliced signals including only the reflected HNSWs within the range of 3.5–4.5 ms. (c) Time-sliced noise-cutting signals, generated by Eq. (2), including only reflected HNSWs without noise.

represents the incident HNSW, generated by the impact of a striker particle, passing through the sensor particle, while the other two peaks correspond to the reflected HNSWs arriving back in the sensor spot after the reflection from the composite sample. Current existing studies [21–23] typically use the amplitudes of the reflected HNSWs and/or the time interval between the incident and the reflected HNSWs as the primary markers to identify the presence of defects in the sample. The main advantage of the proposed DL algorithm is that it can detect defects in real-time by eliminating the burden of manually-analysing such kinds of specific markers.

This study examines three different types of input HNSW signal on the efficiency and accuracy of the detection of defects in an AS4/PEEK composite. The input signals are divided into three types of signals, i.e., original, time-sliced, and time-sliced noise-cutting signals, as shown in Fig. 3. The original signal is the raw HNSW data collected from the sensor without any pre-processing and, therefore it includes both incident and reflected HNSWs, as shown in Fig. 3a. Notice that using the original signals could be beneficial for real-time NDE, because it does not require pre-processing. The time-sliced signal HNSWs, including only the reflected HNSWs, within the range of 3.5–4.5 ms to improve the efficiency of the DL algorithm compared with the original signal. Fig. 3b and c show examples of the time-sliced signal and the time-sliced noise-cutting signal, respectively. In contrast to the original signal, the time-sliced and time-sliced noise-cutting signals require pre-processing achieved by using Eqs. (1) and (2) in Section 3.

Fig. 4 shows the time required for pre-processing of both time-sliced and time-sliced noise-cutting signals. The pre-processing time linearly increases with increasing data for both signals, and pre-processing for the time-sliced noise-cutting takes longer than time-slicing. For real-time NDE, the original signals can be computationally more efficient than these two pre-processed signals because they do not require the pre-processing time.

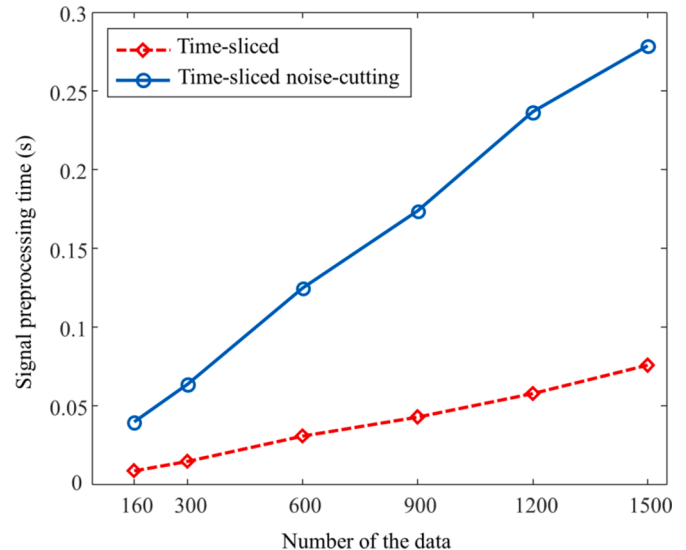


Fig. 4. The pre-processing time to obtain time-sliced (red rhombus dashed line) and time-sliced noise-cutting (blue circle solid line) signals from the original HNSW signals is computed as a function of the number of data.

3. DL design for defect detection

This section describes the CNN architecture specifically designed for the detection of defects in laminated composites using HNSWs as the input data. The CNN gradually extracts local features from high-resolution feature maps, and then combines these features into more abstract feature maps of lower resolution [67]. The CNN architecture proposed in this study for the detection of defects in composites using HNSWs is schematically illustrated in Fig. 5. The proposed CNN

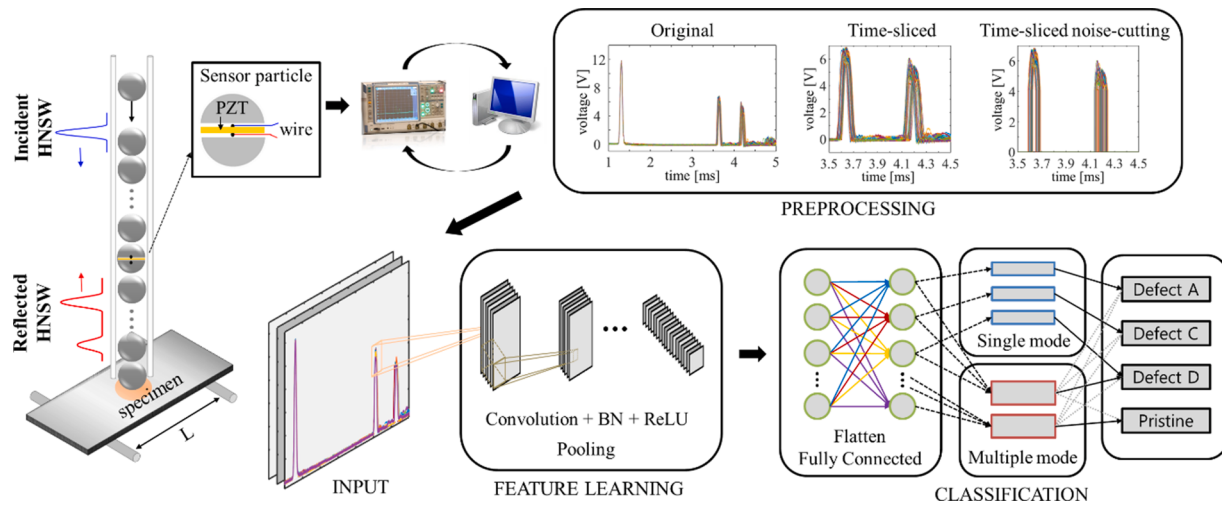


Fig. 5. Architecture of the CNN for defect detection in laminated composites using HNSWs. HNSW signals recorded by the sensor particle are stored in the oscilloscope and used as input signals for deep learning consisting of a pre-processing input layer, a feature extraction neural network, and a classification neural network.

architecture is composed of a data pre-processing input layer, a feature extraction neural network, and a classification neural network. In the following, each layer is briefly explained.

3.1. Data pre-processing input layer

An input layer inputs HNSW signals into a neural network. In this layer, as described in Section 2.3, the time-sliced and time-sliced noise-cutting signals are obtained from pre-processing of the original HNSW signals for the accurate and fast prediction of defects in composites. For an original HNSW signal $V(t)$, the time-sliced input signal can be obtained by

$$X(t) = V(t), \text{ if } t_f - \varepsilon_f \leq t \leq t_s + \varepsilon_s \quad (1)$$

where t_f and t_s can be chosen to include the reflected HNSW signals with positive constants ε_f and ε_s . In this study, we use t_f and t_s as arrival times of the first and secondary reflected HNSWs to the sensor particle and $\varepsilon_f > 0$ and $\varepsilon_s > 2w_s$ with w_s being the width of the secondary reflected HNSW. Based on this, the input signal is time-sliced within the range of 3.5–4.5 ms as shown in Fig. 3b. The time-sliced noise-cutting HNSW signal can be obtained by

$$X(t) = \begin{cases} V(t), & \text{if } V(t) > V_c \\ 0, & \text{otherwise} \end{cases}, \quad t_f - \varepsilon_f \leq t \leq t_s + \varepsilon_s \quad (2)$$

where $V_c > 0$ is a constant that can be chosen to delete noises (see Fig. 3b) occurring within a time $t \in [t_f - \varepsilon_f, t_s + \varepsilon_s]$. Notice that any value greater than the maximum amplitude of the noise can be taken as V_c , i.e., $V_c > \max A$ where A 's are amplitudes of the noise of the reflected HNSWs. Based on this, the noise of the time-sliced signal are deleted by taking $V_c = 4.0$ as shown in Fig. 3c.

3.2. Feature extraction neural network

The feature extraction is achieved by convolution, activation, and pooling layers as shown in Fig. 5. In the convolution layer, certain local features are extracted from the input image by the convolution operation. To obtain a feature output, each input pixel and its corresponding region of the convolution kernel are multiplied by the corresponding set of weights of the convolution kernel. For an input feature map $X \in R^{(m \times n)}$, a filter $F \in R^{(n_w \times n_w)}$, and a bias $B \in R$, the output feature map C^p for a filter p in the convolution layer can be computed by

$$C_{ab}^p = \sum_{c=0}^{n_c} \sum_{i=0}^{n_w} \sum_{j=0}^{n_w} X_{c,sa+i,sb+j} F_{cij}^p + B^p \quad (3)$$

for $0 \leq a, b \leq n_o$ and $0 \leq p \leq n_f$, where n_o is the size of the output feature map, n_f is the number of filter per layer, n_c is the number of channels in the input feature map X is obtained from the original HNSW signal, Eq. (1) for the time-sliced signal, and Eq. (2) for the time-sliced noise-cutting signal. Following the convolution layer, the output feature map passes through a nonlinear activation function. We use a rectified linear unit (ReLU) function and max pooling for down-sampling (or sub-sampling).

3.3. Classification neural network

For classification using the fully connected layer, the output feature map from the feature extraction neural network is vectorised for the input feature map $X \in R^M$. For a weight $W \in R^{(Z \times M)}$, the output of the fully connected layer can be computed as

$$v_z = \sum_{m=0}^M W_{zm} X_m + B_z \quad (4)$$

where z ($0 \leq z \leq Z$) is the number of nodes in the fully connected layer. The softmax layer follows the fully connected layer for classification. For more accurate classification of defects, we developed a new softmax regression, called a multiple mode testing scheme that classifies defects using multiple HNSW signals. The probability of the output can be computed as

$$p(y_i) = \frac{1}{q} \sum_{j=1}^q s_{ij}, \quad s_{ij} = \frac{e^{v_j}}{\sum_{k=1}^m e^{v_k}}, \quad i = 1, \dots, n \quad (5)$$

satisfying $0 \leq p(y_i) \leq 1$. Here, v_j is the weighted sum of the j th output node computed from Eq. (4), n is the number of defect categories, and m is the number of the output nodes. Here, q is the number of HNSW signals used for classification. Notice that if $q = 1$, only one HNSW signal is used for classification, this is called a single mode testing scheme, in this study. In our study, we choose $q = 3$ and $n = 4$ including four categories of defects in composites. A classification layer computes the cross-entropy loss to measure the error of the neural network, and the weights are adjusted by reducing the error of the training data in the supervised learning of the neural network.

4. Results and discussion

The HNSW-based DL algorithm described in the previous section is trained and tested for defect detection in AS4/PEEK laminated composites. The algorithm is tested for both binary and multiple classification neural networks. With the binary classification neural network, we examine the capability of the algorithm to identify the presence of defects in a composite. In contrast, with the multiple classification neural network, we investigate if the algorithm can distinguish the position of defects at three different interface locations through the thickness, as illustrated in Fig. 1b. The number of hidden layers in the CNN is one of most important parameters when optimizing a machine learning system. Therefore, the performance of the algorithm is investigated for various numbers of hidden layers for all three types of input signals. To do so, we generate five trained CNN algorithms for five different numbers of hidden layers via training data and their accuracy is evaluated via testing data. Moreover, we investigate the effects of various CNN internal parameters, such as learning rate, dropout, input image size, filter size, and batch size. Finally, the proposed CNN algorithm is compared with artificial neural network (ANN) and AlexNet.

4.1. Identification of defect presence

To identify the presence of the defect in AS4/PEEK composites, we use a binary classification neural network, which classifies the input data into one of the two groups, i.e., pristine or defect. If there is a defect in the sample, it belongs to a defect group. Otherwise, it belongs to a pristine group. A total of 120 datasets, consisting of 60 randomly-selected datasets from defect-containing samples and 60 from a pristine sample is used as the input data to generate a trained CNN algorithm. The input data are randomly divided into three sets: 70% for training, 15% for validation, and 15% for testing. The training set is used for computing the gradient and updating the network weights and biases. Trained CNN algorithms are generated for different number of hidden layers, i.e., 1, 3, 5, 10, and 20.

In Fig. 6a, an example of the training performance of the CNN algorithm with 10 hidden layers for the time-sliced noise-cutting signal is displayed. Although the training performance for other cases of signal and hidden layers are not shown, it is worth noting that these trends are similar to the performance in Fig. 6a. The performance is measured using cross-entropy loss between network predictions and the known

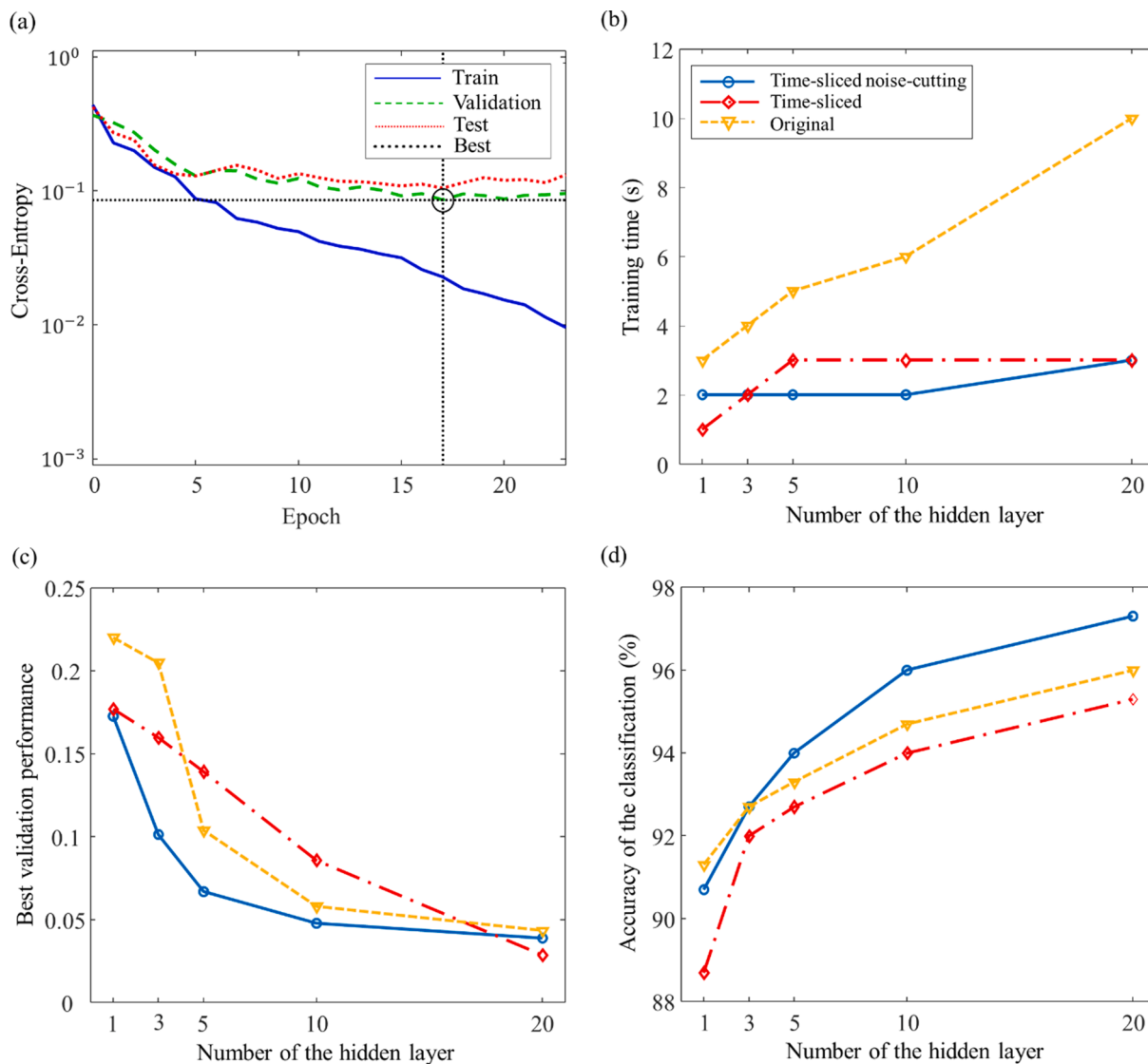


Fig. 6. Training performance and the effect of the number of hidden layers for the classification of defects and pristine sample. (a) Training (blue solid), validation (green dashed), and test (red dotted) losses are measured by cross-entropy for 10 hidden layers and the time-sliced noise-cutting signal. The best validation performance (black circle) is 0.085844 at epoch 17. The effect of the hidden layer is shown on (b) training time, (c) best validation performance, and (d) accuracy for the original (yellow triangle), time-sliced (red rhombus), and time-sliced noise-cutting (blue circle) signals.

correct outputs. Notice that minimizing cross-entropy leads to a good classification, i.e., smaller values give a better classification, and a value of 0 means no misclassification and 100 indicates maximum misclassification. In the figure, the validation error in the training set monotonically decreases. As with the training set error, the error in the validation set decreases during the initial phase of training. However, the validation error starts to rise at epoch 17 due to overfitting. The best validation performance occurs at epoch 17 with a minimum in the validation set error of approximately 0.086. Weights and biases of the network are saved at the minimum of the validation set error. The error in the testing set is higher than the errors in the validation and training testing sets, as expected. Notice that testing has no effect on training, and thus it provides an independent measure of the network performance during and after training.

The important parameters or constraints for a neural network from learning to output production are time complexity and accuracy [67]. Time complexity indicates the time required for a neural network to learn the entire problem, to produce outputs within a given time span. The selection of the number of hidden layers is challenging because it can give rise to a condition of underfitting or overfitting, which can greatly influence the accuracy and time complexity of the network.

To study time complexity and accuracy of the proposed CNN algorithm, we examined the effect of the number of hidden layers on the training time and validation performance for all three input signals in Fig. 6. In Fig. 6b, for the original signal, the training time increases as the number of hidden layers increases. On the other hand, there is no significant increase in training time as the number of hidden layers is increased in both time-sliced and time-sliced noise-cutting signals. The results clearly show that using the original signal requires a greater training time than the other two time-sliced signals due to the relatively large number of data points. In Fig. 6c, the effect of varying the number of hidden layers is investigated in terms of the validation performance based on cross-entropy. It shows a decrease in cross-entropy with an increasing number of hidden layers for all three signals, indicating an improvement in accuracy when a large number of hidden layers are considered. This is consistent with a previous study, where it was shown that high accuracy could be achieved with networks having a large number of hidden layers, even for large complex problems [68].

To evaluate the performance of the trained CNN algorithms with five different hidden layers, we randomly select 150 HNSW data, including 75 from the defect-containing samples and 75 from the pristine samples. This is achieved using a confusion matrix that is a specific technique to summarize or visualize the performance of a classification algorithm in machine learning, typically a supervised learning based authentication [69]. In Table 1, for example, the confusion matrix for the case of 10 hidden layers is shown for the time-sliced signal. In the table, 67 signals out of 75 are correctly classified as signals from the defect-containing samples and 74 signals out of 75 are correctly classified as signals from the pristine samples, i.e., without defect. The accuracy of classification for detecting defects is 94%. The overall classification accuracy of the algorithm is obtained by computing the ratio of the correct predicted HNSWs to the total input HNSWs, i.e., Accuracy = (Corrected predictions/Total predictions) × 100, where the correct predictions are computed by adding all the diagonals in the confusion matrices.

In Fig. 6d, the variation of accuracy with the number of hidden layers is visualized for three different HNSW input signals. As expected, the accuracy is improved when the number of hidden layers is increased.

Table 1
Confusion matrix for classification of defect and pristine.

150 HNSWs(75 per each)		Actual HNSWs	
		Defect	Pristine
Predicted HNSWs	Defect	67	1
	Pristine	8	74
Accuracy		94%	

Interestingly, a high degree of accuracy is achieved even with one hidden layer. This is because binary classification is linearly separable. A relatively high classification accuracy is obtained with the time-sliced noise-cutting signals than the other two signals, highlighting an improvement in accuracy with noise-cutting. Moreover, the time-sliced signals also improve accuracy of the classification relative to the original signals. High accuracy of over 90% can be achieved for all three signals, indicating the possibility of using all three signals as the input data.

4.2. Identification of defect location

As illustrated in Fig. 1b, the defects in the composite samples are located at different positions through the depth of the composite samples. In this section, we examine the capability of the proposed CNN algorithm to distinguish the location of the defect in the composites. In contrast to binary classification in the previous section, this is performed using a multiclass classification neural network that classifies the input data into four classes. The input dataset has four class labels, namely defect A, defect B, and defect C depending on the defect location as illustrated in Fig. 1b and pristine D without a defect. As with the case for the binary classification, five CNN training algorithms with different numbers of hidden layers are generated. A total of 180 HNSW datasets, consisting of 45 from each of four groups, are used to generate such trained CNN algorithms. The input data are randomly divided into 70% for training, 15% for validation, and 15% for testing. The algorithm is tested using two testing methods: single mode testing and multiple mode testing. Single mode testing indicates that the detection is determined by one reflected HNSW signals. Multiple mode testing means that the defects are determined by multiple HNSWs to improve the accuracy of the detection.

In Fig. 7a, the training performance of the CNN algorithm is presented for the case of 10 hidden layers with the time-sliced noise-cutting signal and the single mode testing. Notice that the training performance for the other cases is also similar, although they are not presented. The performance for training, validation and testing is similar to the case of the binary classification neural network in the previous section. The validation error decreases until it reaches a minimum value of around 0.039 at epoch 15, where the network starts overfitting the data. Notice that we obtained a similar training performance for the multiple mode testing. In Fig. 7, the sensitivity of the trained CNN algorithm, in terms of accuracy and efficiency on the number of hidden layers, is examined for the single mode testing. Increasing the number of hidden layers increases training time, and it results in high accuracy as shown in Fig. 7c. The use of the original signal as input shows a higher time complexity than the time-sliced and time-sliced noise-cutting signals due to the use of the whole signal without time slicing.

The trained CNN algorithms with different numbers of hidden layers were tested using a 300 HNSW dataset composed of 75 datasets from each of the four samples. In Tables 2 and 3, we display the confusion matrices to compare the accuracy of the single mode testing with the multiple mode testing for 3 hidden layers and the time-sliced signals. For the single mode testing, 268 out of 300 correctly predict the location of the defect, and it results in 89.3% accuracy. The accuracy might not be sufficiently high, but it is noted that finding defects using a single signal is not an easy task. The multiple mode detection procedure is designed to improve the accuracy of the detection of defects. Multiple mode testing is performed using 100 time sliced HNSWs and 3 HNSW datasets instead of a single one are used to determine the presence of defects in one AS4/PEEK composite. The confusion matrix based on multiple mode testing is also shown in Table 3. The matrix shows that 97 out of 100 HNSW datasets are accurately predicted, indicating 97% accuracy. This result proves that the detection of defect in composites can be more improved by using multiple mode testing rather than single mode testing.

In Fig. 7d, we display the accuracy of the trained CNN algorithms for both single and multiple mode testing. The trend is similar for all three types of signals. While the overall accuracy with more than 3 hidden

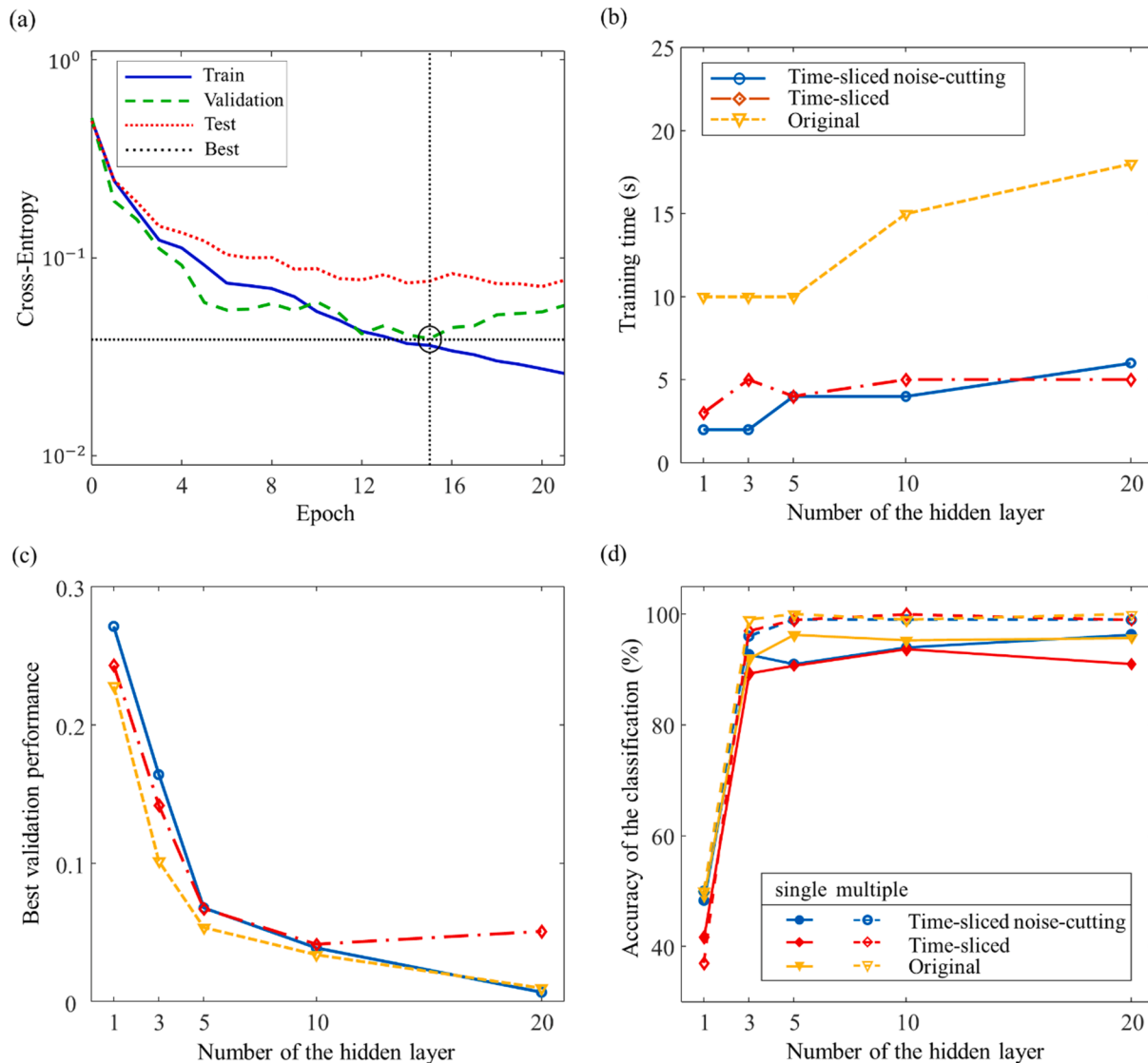


Fig. 7. Training performance and the effect of the hidden layer for the classification of defect location. (a) Training (blue solid), validation (green dashed), and test (red dotted) losses are measured by cross-entropy for 10 hidden layers and the time-sliced noise-cutting signal. The best validation performance (black circle) is 0.038918 at epoch 15. The effect of increasing the number of hidden layers is shown on (b) training time, (c) best validation performance, and (d) classification accuracy for the original (yellow triangle), time-sliced (red rhombus), and time-sliced noise-cutting (blue circle) signals.

Table 2
Confusion matrix for the single mode testing.

300 HNSWs(75 per each)		Actual HNSWs			
		A	B	C	D
Predicted HNSWs	Defect A	73	4	0	12
	Defect B	1	58	1	0
	Defect C	0	6	74	0
	Pristine (D)	1	7	0	63
Accuracy		89.3%			

Table 3
Confusion matrix for the multiple mode testing.

100 HNSWs(x3 per each)		Actual HNSWs			
		A	B	C	D
Predicted HNSWs	Defect A	23	0	0	0
	Defect B	0	24	0	0
	Defect C	0	0	25	0
	Pristine (D)	2	1	0	25
Accuracy		97%			

layers is mostly over 90%, it is very low with 1 hidden layer because multiple classification is linearly inseparable. Regardless of the type of signals, higher accuracy is achieved with more hidden layers for both single and multiple testing modes. The results clearly show the improvement in accuracy with the multiple mode testing. Unlike binary classification, for the single mode testing, its accuracy for three signals is variable with the number of hidden layers and higher accuracy is observed for the original input signal, indicating the possibility of the real-time application of the proposed DL-based sensor. Average accuracies for the single mode testing are approximately 94%, 91%, and 95% for the time-sliced noise cutting, time-sliced, and original signals, respectively.

4.3. Effects of the CNN parameters

This section investigates the effects of various CNN internal parameters on classification accuracy. For this study, we consider the identification of defect location in composites for single mode testing with the time-sliced noise cutting signal.

In Fig. 8, the influence of learning rate is examined for four cases of

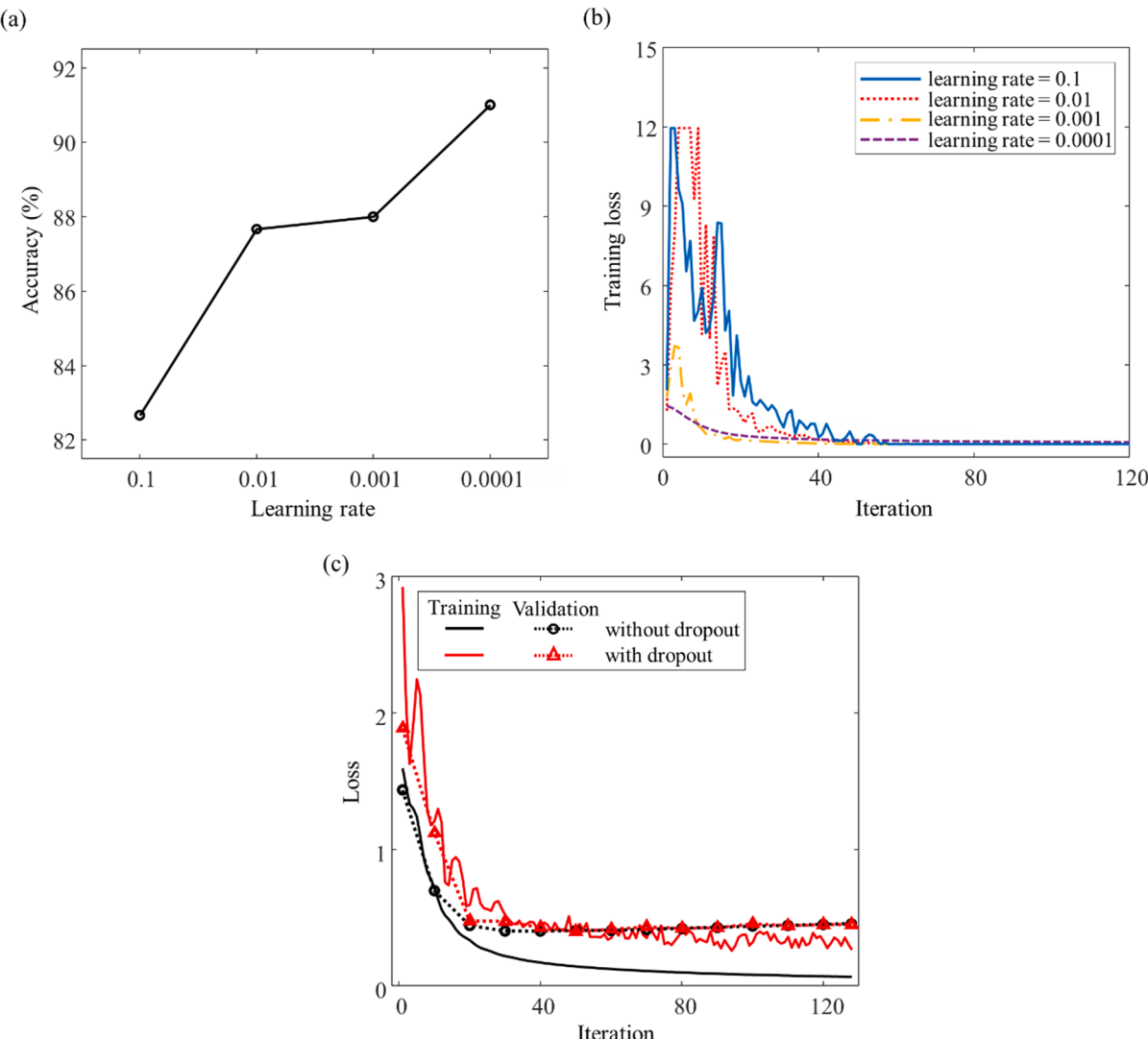


Fig. 8. The effect of learning rate on (a) accuracy and (b) training loss computed for the learning rates of 0.1 (blue solid), 0.01 (red dotted), 0.001 (yellow dashed-dot), and 0.0001(purple dashed). (c) Training and validation losses are shown with 35% dropout (black solid and dotted circle lines) and without dropout (red solid and dotted triangle lines).

learning rates. For the tested learning rates, the accuracy is improved with reducing learning rates with highest accuracy of 91% and a stable training process as shown in Fig. 8b at a learning rate of 0.0001. Moreover, the effects of different activation functions are examined in Table 4. Higher accuracy is obtained with ReLU than Sigmoid and Tanh for both 3 and 5 hidden layers. Based on these findings, unless otherwise specified, all other studies are performed using the learning rate of 0.0001 and ReLU in this study.

Dropout is a regularization approach that randomly discards connections from previous layers during neural network training [70]. Adding the dropout layer is to minimize overfitting within a trained network [71]. In this study, we investigate the effect of overfitting by using a single dropout layer connected to a fully connected layer. As shown in Table 5, the accuracy is over 90% regardless of the existence of

Table 4
Effect of activation function.

Activation Function	Accuracy (%)	
	3 hidden layers	5 hidden layers
ReLU	90.7	91
Sigmoid	87.7	81.7
Tanh	89	84.3

Table 5
Effect of dropout rate.

Dropout rate (%)	Accuracy (%)	
	3 hidden layers	5 hidden layers
0 (without Dropout)	90.7	91
20	92.3	91.7
35	92	90.7
50	90.7	91

the dropout layer, indicating less sensitivity of the proposed DL algorithm to dropout. Fig. 8c shows the training and validation loss according to the 35% dropout rate and without dropout for 5 hidden layers. As training proceeds without dropout, overfitting is confirmed by the difference between training loss and validation loss. Although the use of dropout increases training loss, it can help prevent overfitting.

The HNSW signal obtained through data processing is converted into an input image. In Fig. 9a, we examine the effect of the pixel size of the input image for 5 hidden layers. The accuracy is significantly increased from 66 to 92% when the pixel size is increased from 101×101 to 401×401 . However, if the pixel size is larger than 401×401 , training time increases and the accuracy decreases. In Fig. 9b, the effect of the filter

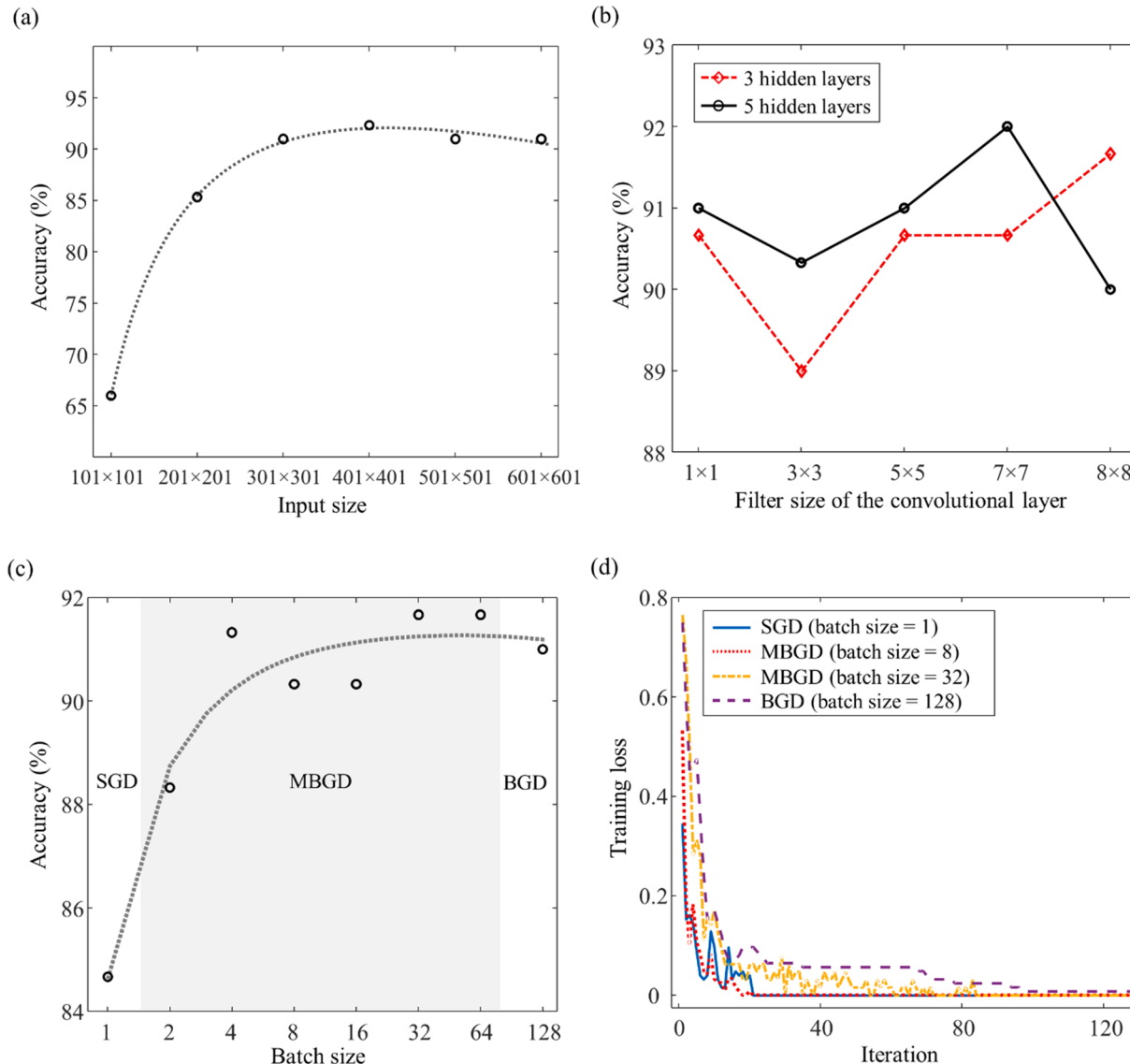


Fig. 9. (a) Classification accuracy (circles) vs. pixel size of the input image for 5 hidden layers. The dotted curve is the fitting curve from Eq. (8), representing the relationship between the input pixel size and accuracy. (b) Classification accuracy vs. the filter size of the convolutional layer for 3 (red rhombus dashed) and 5 (black circled solid) hidden layers. (c) Classification accuracy (circles) is shown for various gradient descent techniques: stochastic gradient descent (SGD, batch size = 1), batch gradient descent (BGD, batch size = 128), and mini batch gradient descent (MBGD, $1 < \text{batch size} < 128$). The dotted line is the fitting curve from Eq. (8), representing the relation between the batch size and the accuracy. (d) Training losses are shown for SGD (blue solid), MBGD (red dotted, batch size = 8), MBGD (yellow dash-dotted, batch size = 32), and BGD (purple dashed, batch size = 128).

size of the convolution layer is studied for 3 and 5 hidden layers with a stride of 1. The accuracy of classification ranges from 89 to 92%, indicating less sensitivity with a variation of the filter size.

We compare different gradient descent techniques such as stochastic gradient descent (SGD, batch size = 1), batch gradient descent (BGD, batch size = 128), and mini batch gradient descent (MBGD, $1 < \text{batch size} < 128$) using 128 HNSW input data. Fig. 9c shows the accuracy according to the batch size, and the horizontal axis is plotted on a log-scale for visual convenience. The SGD has the lowest accuracy of 84.67%. The highest accuracy of 91.67% is obtained from the MBGD with batch sizes of 32 and 64. This result shows that using the batch can increase the accuracy of the classification. Moreover, as shown in Fig. 9d, the SGD curve has large fluctuations in the training loss and the BGD curve is relatively smooth. The MBGD curves lie between the SGD and BGD curves and show small fluctuations. As expected, the SGD yields faster reduction in the training loss than BGD and MBGD, highlighting the faster learning of the SGD.

To obtain high accuracy with proper choices of the input pixel and batch sizes, we establish a relation between the accuracy and the pixel or batch size through a general fitting curve

$$y = \left(\frac{ax^2 + bx + c}{x + d} \right) \times 100 \quad (8)$$

where x represents either input size or batch size, and y is accuracy, and a , b , c , and d are fitting parameters obtained from a least square fit to

Table 6
Fitting parameters.

Fitting parameters	Input pixel size	Batch size
a	-0.0002846	-0.00001732
b	1.163	0.9145
c	-39.46	-0.3598
d	12.85	-0.3446

classification accuracy (black circles) as listed in Table 6. These fitting curves (dotted lines) are included in Fig. 9a and c. They can be used as a reference curve to infer the effective parameters for accuracy.

4.4. Comparison of CNN architectures

The proposed CNN algorithm is compared with ANN and AlexNet in the single mode testing for the time-sliced noise-cutting signal. In this study, ANN uses the fully connected layer with a dropout of 20% and the ReLU activation function. As one of the pre-trained CNN algorithms, AlexNet [40] consists of 5 convolutional layers and 3 fully connected layers with the ReLU activation function.

In Fig. 10, we compare the accuracy of classification for CNN, ANN, and AlexNet with/without batch normalization. Without batch normalization, the accuracy of the CNN is over 90%, which is higher than those of ANN and AlexNet. On the other hand, the accuracy for all three models is improved with batch normalization. Importantly, regardless of batch normalization, high accuracy of over 90% can be achieved with the proposed CNN architecture in this study. The accuracy of AlexNet is significantly improved, i.e., about 9.33%, with batch normalization, but the slight increase of the accuracy for both CNN and ANN is observed. This result indicates that the CNN and AlexNet with batch normalization has better precision compared to ANN or architectures without batch normalization.

5. Conclusion

We introduced a novel NDE technique for real-time detection of defects in laminated composites by incorporating a CNN based DL algorithm into a granular crystal sensor. To verify the performance of the proposed DL algorithm, it was trained and tested for the identification of the presence and location of delamination in AS4/PEEK laminated composites using three different input signals, namely the original (without pre-processing), time-sliced and time-sliced noise cutting signals (with pre-processing). The influence of using various CNN parameters including a hidden layer were investigated to improve the accuracy of the proposed algorithm.

The presence of defects in AS4/PEEK composites was identified with the binary classification neural network. It was found that, for all three input signals, the classification accuracy could be increased by increasing the number of hidden layers and an accuracy of over 90% was achieved by using more than three hidden layers. Moreover, a relatively high level of accuracy was obtained using time-sliced noise-cutting signals. The ability of the CNN algorithm to identify the location of delaminations in AS4/PEEK composites was verified using a multiclass classification neural network. While a high accuracy of over 90% was achieved for both single and multiple mode testing schemes for all three input signals, a higher accuracy prediction was achieved using the multiple mode testing scheme. Interestingly, there was no significant difference in the accuracy for time-sliced noise cutting and original input signals, indicating that the original input signal can be used for real-time prediction of defects in composites. These results show that the proposed HNSW based DL algorithm can achieve high accuracy in the detection of defects in laminated composites with a lower number of the hidden layers for all tested three signals.

In addition to the effect of the hidden layer, the sensitivity of other CNN internal parameters on the accuracy was examined for the identification of the defect location using a single mode testing scheme with time-sliced noise-cutting signals. It was found that there was no significant change in accuracy with the variation of dropout rates, ranging from 0 to 50% and the filter sizes of the convolution layer. On the other hand, the classification accuracy could be improved by reducing the learning rate, increasing the pixel size in the input image, and by using batch normalization and the ReLU activation function. The highest accuracy was observed for a learning rate of 0.0001, a batch size of 32 and 64, and an input pixel size of 401×401 . Moreover, the proposed CNN

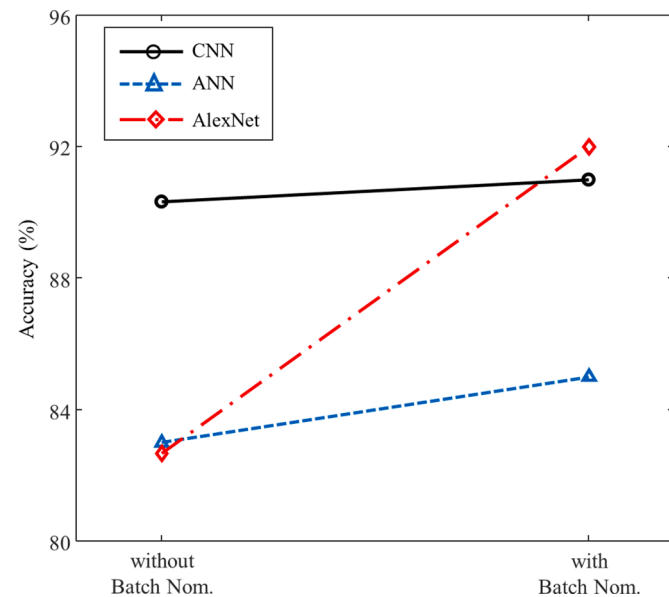


Fig. 10. The classification accuracy of the proposed CNN architecture is compared with those associated with the ANN and AlexNet approaches both with and without batch normalization. The black circle, blue triangle, and red rhombus represent the accuracies of the CNN, ANN, and AlexNet, respectively.

algorithm was compared to ANN and AlexNet with and without batch normalization. Unlike the ANN and AlexNet approaches, an accuracy of over 90% was achieved with the current CNN algorithm, regardless of the use of batch normalization.

Although the proposed DL algorithm was only used to detect delamination in AS4/PEEK laminated composites in this study, it could be applied to other problems where the granular crystal sensor has been successfully applied so far. Based on this, future work would focus on applying it to NDE of other types of composite materials and defects such as voids, weak bonds, disbonds, cracks, localized corrosion and the characterization of the mechanical properties of materials and structures including composites, rocks, and compacted materials. Moreover, further verification and improvement of the sensitivity of the granular crystal sensor would be necessary for the applications of the solitary wave based DL algorithm to other types of scientific problems.

CRediT authorship contribution statement

Sangyoung Yoon: Investigation, Formal analysis, Software, Writing – original draft, Validation, Writing – review & editing, Visualization. **Amang (Song-Kyoo) Kim:** Methodology, Investigation, Software, Writing – original draft. **Wesley J. Cantwell:** Writing – review & editing, Methodology, Investigation. **Chan Yeob Yeun:** Methodology, Writing – review & editing. **Chung-Suk Cho:** Writing – review & editing. **Young-Ji Byon:** Writing – review & editing. **Tae-Yeon Kim:** Conceptualization, Funding acquisition, Methodology, Investigation, Project administration, Supervision, Validation, Writing – original draft, Writing – review & editing.

Declaration of Competing Interest

The authors declare that they have no known competing financial interests or personal relationships that could have appeared to influence the work reported in this paper.

Data availability

No data was used for the research described in the article.

Acknowledgements

The authors acknowledge support from Khalifa University Awards No. CIRA-2019-009, No. RCII-2019-003, and the Center for Cyber-Physical Systems, Khalifa University, under Grant Number 8474000137-RC1-C2PS-T3. This research was also performed as part of the Advanced Research and Innovation Center (ARIC) program which is jointly-funded by STRATA Manufacturing PJSC (a Mubadala company) and Khalifa University.

References

- [1] Amran YM, Alyousef R, Rashid RS, Alabduljabbar H, Hung CC. Properties and applications of FRP in strengthening RC structures: a review. *Structures*, 16. Elsevier; 2018.
- [2] Muhammad A, Rahman MR, Baini R, Bakri MKB. Applications of sustainable polymer composites in automobile and aerospace industry. *Advances in sustainable polymer composites*. Woodhead Publishing; 2021. p. 185–207.
- [3] Sun CT, Yoon KJ. Characterization of elastic-plastic behavior of an AS4/PEEK thermoplastic composite for temperature variation. *J Compos Mater* 1991;25: 1297–313.
- [4] Maekawa Z, Hamada H, Lee K, Kitagawa T. Reliability evaluation of mechanical properties of AS4/PEEK composites. *Composites* 1994;25(1):37–45.
- [5] Brotherhood CJ, Drinkwater BW, Dixon S. The detectability of kissing bonds in adhesive joints using ultrasonic techniques. *Ultrasonics* 2003;41:521–9.
- [6] Kumar RLV, Bhat MR, Murthy CR. Some studies on evaluation of degradation in composite adhesive joints using ultrasonic techniques. *Ultrasonics* 2013;53: 1150–62.
- [7] Singher L, Segal Y, Segal E, Shamir J. Considerations in bond strength evaluation by ultrasonic guided waves. *J Acoust Soc Am* 1994;96:2497–505.
- [8] Malinowski P, Wandowski T, Ostachowicz W. The use of electromechanical impedance conductance signatures for detection of weak adhesive bonds of carbon fibre-reinforced polymer. *Struct Health Monit* 2015;14:332–44.
- [9] Yang S, Gu L, Gibson RF. Nondestructive detection of weak joints in adhesively bonded composite structures. *Compos Struct* 2001;51:63–71.
- [10] Roach D, Rackow K, Duvall R. Innovative use of adhesive interface characteristics to nondestructively quantify the strength of bonded joints. In: Proceedings of the 10th European conference on non-destructive testing; 2010. p. 3263–77.
- [11] Bossi R, Housen K, Shepherd W. Using shock loads to measure bonded joint strength. *Mater Eval* 2002;60:1333–8.
- [12] Kumar RLV, Bhat MR, Murthy CR. Evaluation of kissing bond in composite adhesive lap joints using digital image correlation: preliminary studies. *Int J Adhes Adhes* 2013;42:60–8.
- [13] Yang J, Silvestro C, Khatri D, De Nardo L, Daraio C. Interaction of highly nonlinear solitary waves with linear elastic media. *Phys Rev E* 2001;83:046606.
- [14] Khatri D, Rizzo P, Daraio C. Highly nonlinear waves' sensor technology for highway infrastructures. In: Proceedings of the SPIE smart structures/nondestructive evaluation and health monitoring; 2008. 6934–25.
- [15] Xianglei N, Rizzo P, Daraio C. Actuators for the generation of highly nonlinear solitary waves. *Rev Sci Instrum* 2011;82:034902.
- [16] Nesterenko VF. Dynamics of heterogeneous materials. New York: Springer-Verlag; 2001.
- [17] Daraio C, Nesterenko VF, Herbold EB, Jin S. Strongly nonlinear waves in a chain of Teflon beads. *Phys Rev E* 2005;72(1):016603.
- [18] Daraio C, Nesterenko VF, Herbold EB, Jin S. Tunability of solitary wave properties in one-dimensional strongly nonlinear phononic crystals. *Phys Rev E Stat Nonlinear Soft Matter Phys* 2006;73(2):026610.
- [19] Sen S, Hong J, Bang J, Avalos E, Doney R. Solitary waves in the granular chain. *Phys Rep* 2008;462:21–66.
- [20] Job S, Melo F, Sokolow A, Sen S. How Hertzian solitary waves interact with boundaries in a 1D granular medium. *Phys Rev Lett* 2005;94:178002.
- [21] Singhla T, Kim E, Kim T-Y, Yang J. Weak bond detection in composites using highly nonlinear solitary waves. *Smart Mater Struct* 2017;26:055011.
- [22] Kim E, Restuccia F, Yang J, Daraio C. Solitary wave-based delamination detection in composite plates using a combined granular crystal sensor and actuator. *Smart Mater Struct* 2015;24:125004.
- [23] Schiffer A, Alia RA, Cantwell W, Kim E, Lee D, Kim T-Y. Elastic interaction between nonlinear solitary waves in granular chains and composite beams: experiments and modelling. *Int J Mech Sci* 2020;170:105350.
- [24] Yoon S, Schiffer A, Cantwell WJ, Kim T-Y. Detection of core-skin disbonds in honeycomb composite sandwich structures using highly nonlinear solitary wave. *Compos Struct* 2021;256:113071.
- [25] Wang Y, Shao Z, Zhao J, Wu H. Coupling effect between highly nonlinear solitary waves and composite plate with matrix cracking. *Compos Struct* 2022;292:115693.
- [26] Schiffer A, Alkhaja AL, Yang J, Esfahani EN, Kim T-Y. Interaction of highly nonlinear solitary waves with elastic solids containing a spherical void. *Int J Solids Struct* 2017;118–119:204–12.
- [27] Ni X, Rizzo P. Highly nonlinear solitary waves for the inspection of adhesive joints. *Exp Mech* 2012;52:1493–501.
- [28] Ni X, Rizzo P, Yang J, Khatri D, Daraio C. Monitoring the hydration of cement by means of highly nonlinear solitary waves. *NDT E Int* 2012;52:76–85.
- [29] Yang J, Sangiorgio SN, Borkowski SL, Silvestro C, De Nardo L, Daraio C, Ebramzadeh E. Site-specific quantification of bone quality using highly nonlinear solitary waves. *J Biomech Eng* 2012;134:101001.
- [30] Yoon S, Schiffer A, Kim JJ, Jang IG, Lee S, Kim T-Y. Numerical predictions of the interaction between highly nonlinear solitary waves and the microstructure of trabecular bone in the femoral head. *J Mech Behav Biomed Mater* 2020;109: 103805.
- [31] Yoon S, Schiffer A, Jang IG, Lee S, Kim T-Y. Predictions of the elastic modulus of trabecular bone in the femoral head and the intertrochanter: a solitary wave-based approach. *Biomech Model Mechanobiol* 2021;20(5):1733–49.
- [32] Kim T-Y, Yoon S, Schiffer A, Jang IG, Lee S. Site-specific quality assessment of trabecular bone using highly nonlinear solitary waves. In: *Lecture Notes in Civil Engineering*. 127. Springer; 2021. p. 893–901.
- [33] Yang J, Silvestro C, Sangiorgio SN, Borkowski SL, Ebramzadeh E, De Nardo L, Daraio C. Nondestructive evaluation of orthopaedic implant stability in THA using highly nonlinear solitary waves. *Smart Mater Struct* 2012;21:012002.
- [34] Jalali H, Rizzo P. Numerical investigation of the interaction of highly nonlinear solitary waves with corroded steel plates. *Int J Mech Sci* 2021;208:106676.
- [35] Jalali H, Misra R, Dickerson SJ, Rizzo P. Detection and classification of corrosion-related damage using solitary waves. *Res Nondestruct Eval* 2022;33(2):78–97.
- [36] Jalali H, Misra R, Dickerson SJ, Rizzo P. Remote wireless monitoring of localized corrosion using compact solitary waves. *Struct Health Monit* 2022. In press.
- [37] Schiffer A, Kim T-Y. Modelling of the interaction between nonlinear solitary waves and composite beams. *Int J Mech Sci* 2019;151:181–91.
- [38] Schiffer A, Lee D, Kim E, Kim T-Y. Interaction of highly nonlinear solitary waves with rigid polyurethane foams. *Int J Solids Struct* 2018;152–153:39–50.
- [39] Koza JR, Bennett FH, Andre D, Keane MA. Automated design of both the topology and sizing of analog electrical circuits using genetic programming. *Artificial intelligence in design*, 96. Dordrecht: Springer; 1996. p. 151–70.
- [40] Krizhevsky A, Sutskever I, Hinton GE. Imagenet classification with deep convolutional neural networks. In: *Proceedings of the advances neural information processing systems*; 2011. p. 1097–105.
- [41] Yu H, Xie T, Hamilton M, Wilamowski B. Comparison of different neural network architectures for digit image recognition. In: *Proceedings of the 4th international conference on human system interactions, HSI*. IEEE; 2011. p. 2011.
- [42] Weiss SM, Kapouleas I. An empirical comparison of pattern recognition, neural nets, and machine learning classification methods. *IJCAI* 1989;89. Vol.
- [43] Szandal T. Comparison of different learning algorithms for pattern recognition with Hopfield's neural network. *Procedia Comput Sci* 2015;71:68–75.
- [44] Van Gerven M, Bohte S. Artificial neural networks as models of neural information processing. *Front Comput Neurosci* 2017;11:114.
- [45] T.A. Straeter, "On the extension of the Davidon-Broyden class of rank one, Quasi-Newton minimization methods to an infinite dimensional hilbert space with applications to optimal control problems". NASA Technical Reports Server. NASA.
- [46] Yoon S, Kim G, Schiffer A, Cantwell WJ, Kim E, Kim T-Y. Detection of delaminations in AS4/PEEK composite plates using highly nonlinear solitary waves. *Compos Struct* 2022;289:115511.
- [47] Masci J, Meier U, Ciresan D, Schmidhuber J, Fricout G. Steel defect classification with max-pooling convolutional neural networks. In: *Proceedings of the international joint conference on neural networks (IJCNN)*. IEEE; 2012.
- [48] Medai D, Posilović L, Subasić M, Budimir M, Lončarić S. Automated defect detection from ultrasonic images using deep learning. *IEEE Trans Ultrason Ferroelectr Freq Control* 2021;68(10):3126–34.
- [49] Faghih-Roohi S, Hajizadeh S, Núñez A, Babuska R, De Schutter B. Deep convolutional neural networks for detection of rail surface defects. In: *Proceedings of the international joint conference on neural networks (IJCNN)*. IEEE; 2016.
- [50] Yuan H, Chen H, Liu S, Lin J, Luo X. A deep convolutional neural network for detection of rail surface defect. In: *Proceedings of the IEEE vehicle power and propulsion conference (VPPC)*. IEEE; 2019.
- [51] Cui X, Liu Y, Zhang Y, Wang C. Tire defects classification with multi-contrast convolutional neural networks. *Int J Pattern Recognit Artif Intell* 2018;32(04): 1850011.
- [52] Hou W, Wei Y, Guo J, Jin Y. Automatic detection of welding defects using deep neural network. *J Phys Conf Ser* 2017;933(1). IOP Publishing.
- [53] Zhu P, Cheng Y, Banerjee P, Tamburrino A, Deng Y. A novel machine learning model for eddy current testing with uncertainty. *NDT E Int* 2019;101:104–12.
- [54] Meng M, Chua YJ, Wouterson E, Ong CPK. Ultrasonic signal classification and imaging system for composite materials via deep convolutional neural networks. *Neurocomputing* 2017;257:128–35.
- [55] Cui R, Azuara G, Lanza di Scalea F, Barrera E. Damage imaging in skin-stringer composite aircraft panel by ultrasonic-guided waves using deep learning with convolutional neural network. *Struct Health Monit* 2022;21(3):1123–38.
- [56] Mardanshahi A, Nasir V, Kazemirad S, Shokrieh MM. Detection and classification of matrix cracking in laminated composites using guided wave propagation and artificial neural networks. *Compos Struct* 2020;246:112403.
- [57] Sammons D, Winfree WP, Burke E, Ji S. Segmenting delaminations in carbon fiber reinforced polymer composite CT using convolutional neural networks. *AIP Conf Proc* 2016;1706(1). AIP Publishing LLC.
- [58] Zhang D, Liu Y, Liu H, Feng Y, Guo H, Hong Z, Chen C, Zhang Y. Characterisation of damage evolution in plain weave SiC/SiC composites using in situ X-ray micro-computed tomography. *Compos Struct* 2021;275:114447.
- [59] Gong Y, Luo J, Shao H, Li Z. A transfer learning object detection model for defects detection in X-ray images of spacecraft composite structures. *Compos Struct* 2022; 284:115136.

- [60] Sikdar S, Liu D, Kundu A. Acoustic emission data based deep learning approach for classification and detection of damage-sources in a composite panel. Compos Part B Eng 2022;228:109450.
- [61] Barile C, Casavola C, Pappalettera G, Kannan VP. Damage monitoring of carbon fibre reinforced polymer composites using acoustic emission technique and deep learning. Compos Struct 2022;292:115629.
- [62] Xu D, Liu PF, Chen ZP. A deep learning method for damage prognostics of fiber-reinforced composite laminates using acoustic emission. Eng Fract Mech 2022;259:108139.
- [63] Luo Q, Gao B, Woo WL, Yang Y. Temporal and spatial deep learning network for infrared thermal defect detection. NDT E Int 2019;108:102164.
- [64] Marani R, Palumbo D, Galietti U, D'Orazio T. Deep learning for defect characterization in composite laminates inspected by step-heating thermography. Opt Lasers Eng 2021;145:106679.
- [65] Bang HT, Park S, Jeon H. Defect identification in composite materials via thermography and deep learning techniques. Compos Struct 2020;246:112405.
- [66] Al Hammadi A, Lee D, Yeun CY, E Damiani, Kim SK, Yoo PD, Choi HJ. Novel EEG sensor-based risk framework for the detection of insider threats in safety critical industrial infrastructure. IEEE Access 2020;8:206222–34. <https://doi.org/10.1109/ACCESS.2020.3037979>. 16 November.
- [67] Roopa CK, Harish BS. A survey on various machine learning approaches for ECG analysis. Int J Comput Appl 2017;163:25–33.
- [68] Uzair M, Jamil N. Effects of hidden layers on the efficiency of neural networks. In: Proceedings of the IEEE 23rd international multitopic conference (INMIC); 2020. 5–7 Nov.
- [69] Kim SK, Yeun CY, Damiani E, Lo NW. A machine learning framework for biometric authentication using electrocardiogram. IEEE Access 2019;7:94858–68.
- [70] Awan S, Riaz M, Khan A. Prediction of heart disease using artificial neural network. VFAST Trans Softw Eng 2018;13.
- [71] Srivastava N, Hinton G, Krizhevsky A, Sutskever I, Salakhutdinov R. Dropout: a simple way to prevent neural networks from overfitting. J Mach Learn Res 2014;15 (1):1929–58.